

THz conductivity of $\text{Sr}_{1-x}\text{Ca}_x\text{RuO}_3$

Diana Geiger,^{1,2} Uwe S. Pracht,¹ Martin Dressel,¹ Jernej Mravlje,³

Melanie Schneider,⁴ Philipp Gegenwart,^{4,*} and Marc Scheffler^{1,†}

¹*1. Physikalisches Institut, Universität Stuttgart, D-70569 Stuttgart, Germany*

²*Institut für Festkörperphysik, Technische Universität Wien, A-1040 Vienna, Austria*

³*Jozef Stefan Institute, SI-1000, Ljubljana, Slovenia*

⁴*I. Physikalisches Institut, Georg-August-Universität, D-37073 Göttingen, Germany*

(Dated: September 10, 2018)

We investigate the optical conductivity of $\text{Sr}_{1-x}\text{Ca}_x\text{RuO}_3$ across the ferromagnetic to paramagnetic transition that occurs at $x = 0.8$. The thin films were grown by metalorganic aerosol deposition with $0 \leq x \leq 1$ onto NdGaO_3 substrates. We performed THz frequency domain spectroscopy in a frequency range from 3 cm^{-1} to 40 cm^{-1} (100 GHz to 1.4 THz) and at temperatures ranging from 5 K to 300 K, measuring transmittivity and phase shift through the films. From this we obtained real and imaginary parts of the optical conductivity. The end-members, ferromagnetic SrRuO_3 and paramagnetic CaRuO_3 , show a strongly frequency-dependent metallic response at temperatures below 20 K. Due to the high quality of these samples we can access pronounced intrinsic electronic contributions to the optical scattering rate, which at 1.4 THz exceeds the residual scattering rate by more than a factor of three. Deviations from a Drude response start at about 0.7 THz for both end-members in a remarkably similar way. For the intermediate members a higher residual scattering originating in the compositional disorder leads to a featureless optical response, instead. The relevance of low-lying interband transitions is addressed by a calculation of the optical conductivity within density functional theory in the local density approximation (LDA).

I. INTRODUCTION

The optical response of a material provides access to its electronic behavior in a broad window of energy scales¹. High-frequency ultraviolet and visible light spectroscopies probe interband transitions, which give rise to an onset in the frequency-dependent optical absorption, whereas infrared and THz spectroscopies at lower energies provide access to more subtle aspects of the collective low-frequency response of an electron gas. One of the most interesting aspects of the collective behavior are quantum phase transitions (QPTs)^{2,3}. Due to the absence of a characteristic scale near the QPT, one expects the optical response of such a material to be characterized by power laws. Power-law conductivity was found in several quantum-critical materials, such as MnSi ^{1,4} and in cuprates close to optimal doping¹. It was also observed in perovskite ruthenates^{1,5-8}, the subject of the present paper.

The perovskite-structured ruthenate system $\text{Sr}_{1-x}\text{Ca}_x\text{RuO}_3$ is a candidate material for a ferromagnetic QPT⁹⁻¹¹. Its undoped parent compound SrRuO_3 is an itinerant ferromagnet with ordering temperature $T_C = 160 \text{ K}$ and is of great interest for both fundamental physics as well as applications¹², whereas the other parent compound, CaRuO_3 , is a paramagnetic metal. CaRuO_3 has been argued to be close to the magnetic critical point as revealed by $T^{3/2}$ temperature dependence of dc resistivity¹³ below 30 K and logarithmic term in the temperature-dependent specific heat¹⁴. Very recently, the observation of Shubnikov-de-Haas oscillations and T^2 resistivity below 1.5 K revealed that a fragile Fermi liquid is recovered at low temperatures. In SrRuO_3 the Fermi liquid is more robust with T^2

resistivity up to about 10 K^{13,15}.

THz and infrared optical studies on both compounds⁵⁻⁸ revealed an unusual optical response with the optical conductivity $\hat{\sigma}(\omega) = \sigma_1(\omega) + i\sigma_2(\omega)$ distinct from that of the Drude behavior that is given by

$$(1) \quad \sigma_1(\omega) = \sigma_{\text{dc}} \frac{1}{1 + \omega^2 \tau_D^2}$$

$$(2) \quad \sigma_2(\omega) = \sigma_{\text{dc}} \frac{\omega \tau_D}{1 + \omega^2 \tau_D^2}$$

with $\tau_D = 1/\Gamma_D$ the Drude scattering time and $\sigma_{\text{dc}} = 1/\rho_{\text{dc}}$ zero-frequency conductivity¹⁶. A recent optical study on clean CaRuO_3 samples revealed Drude behavior¹⁷ consistent with Fermi liquid concepts, but only up to a frequency of 0.6 THz. Starting from 0.6 THz an abrupt increase of the optical scattering rate was found. A possible origin of this behavior is the coupling to a critical low-energy fluctuation.

A different point of view was offered in a very recent dynamical-mean-field theory study of CaRuO_3 ¹⁸, which pointed out the importance of low-lying interband transitions. Namely, the orthorhombic distortion of the cubic perovskite lattice leads to a series of mini-gaps (with the gap size of the order of THz), which significantly affect the optical response. A related tetragonal ruthenate Sr_2RuO_4 that occurs in a non-distorted structure does not show low-frequency deviations and exhibits a standard Fermi liquid optical response¹⁹, instead. One needs to add however, that Sr_2RuO_4 was also argued to be further away from the quantum critical point¹⁴.

In the present work we address the evolution of the optical response of $\text{Sr}_{1-x}\text{Ca}_x\text{RuO}_3$ as a function of composition, across the magnetic phase transition. We have grown thin films, and for the compositions $x = 0, x =$

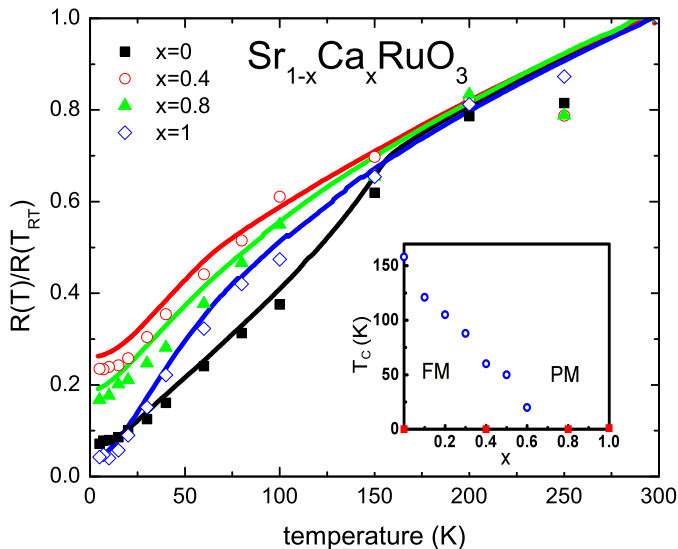


FIG. 1. (color online) Resistivity values, obtained from low-frequency optical data (symbols) and four-point dc measurements (lines). Optical relative resistivity data were calculated from low-frequency (between 4 cm^{-1} and 5 cm^{-1}) THz data by normalizing to the 300 K value, dc data are normalized to the 280 K value. Inset: phase diagram of $\text{Sr}_{1-x}\text{Ca}_x\text{RuO}_3$. Circles represent Curie temperatures of differently doped thin-film samples²⁰, squares indicate the doping levels that were investigated in this optical study.

0.4 , $x = 0.8$ and $x = 1$ (denoted by solid symbols on the phase diagram in the inset of Fig. 1) the THz response was measured. The end-members of the series are sufficiently clean to exhibit optical conductivity that corresponds to a strongly frequency-dependent scattering rate. We investigate the optical response also theoretically within density functional theory in the local-density approximation. The calculated optical scattering rate for both CaRuO_3 and SrRuO_3 shows strong frequency dependence even though frequency-independent scattering is put into the calculation; this suggests the relevance of low-lying interband transitions.

The paper is structured as follows: in Sec. II we present the details of the sample growth and the experimental setup. In Sec. III we show the measured optical conductivities and the associated optical scattering rate. In Sec. IV we present the optical conductivity as calculated within the LDA approximation and discuss the relevance of the interband transitions with respect to the experimental results. In Sec. V we summarize and conclude, and in the Appendix we analyze the scaling properties of the measured conductivities.

II. SAMPLES AND EXPERIMENTAL SETUP

The epitaxial $\text{Sr}_{1-x}\text{Ca}_x\text{RuO}_3$ thin films were grown in Göttingen by metalorganic aerosol deposition (MAD)^{21,22}. We investigated the four different compo-

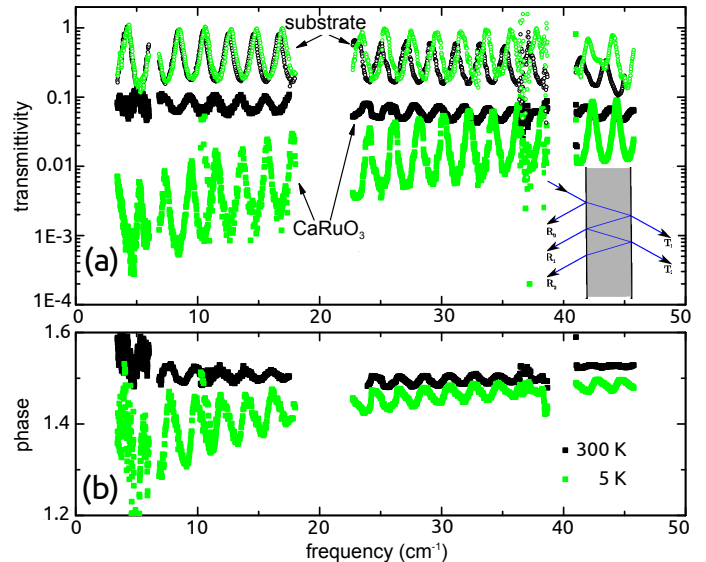


FIG. 2. (color online) Transmittivity (a) and phase (b) data of CaRuO_3 on NdGaO_3 and bare NdGaO_3 substrate at 300 K and 5 K. Open circles correspond to substrate data, full squares to thin-film samples. Inset of (a): multiple reflections in a dielectric substrate lead to Fabry-Pérot oscillations in the raw data.

x	thickness(nm)	T_C (K)	RRR	ρ_{dc} ($\mu\Omega\text{cm}$)	ρ_{THz} ($\mu\Omega\text{cm}$)
0	70	150	15	194	185
0.4	80	60	3.8	259	290
0.8	77	-	5.4	215	230
1	40	-	31	230	237

TABLE I. Properties of the studied thin-film samples. Depending on calcium content x , the table shows: the film thickness, the Curie temperature T_C determined from dc resistivity measurements (derivative), the residual resistivity ratio RRR from $R(300\text{K})/R(0\text{K})$ with a low-temperature extrapolation for the 0 K value, the dc resistivity value at 280 K and the low-frequency THz resistivity value at 300 K (both used in the normalized curves of Fig. 2).

sitions SrRuO_3 , $\text{Sr}_{0.6}\text{Ca}_{0.4}\text{RuO}_3$, $\text{Sr}_{0.2}\text{Ca}_{0.8}\text{RuO}_3$, and CaRuO_3 , all deposited on $\text{NdGaO}_3(110)$ substrates. The thin films grow epitaxially on the substrate with the same [110] orientation. NdGaO_3 is the substrate of choice: its lattice constant matches the thin films well, and its dielectric properties are convenient for transmittivity measurements. More precisely, for SrRuO_3 the substrate leads to 1.7% of compressive strain²³⁻²⁵ and for CaRuO_3 to about -0.4% of tensile strain^{12,17,26}. Our measurements of the lattice constant perpendicular to the substrate are consistent with the results referenced above (not shown). Another popular substrate, SrTiO_3 has a very large frequency- and temperature-dependent dielectric function, which makes optical measurements difficult^{27,28}. Some relevant sample properties are listed in table I. All four samples are of high quality and clearly

metallic, as evident from the resistivity curves and residual resistivity ratios (RRR) between 300 K and 0 K (extrapolated value) in Fig. 1 and table I. While the SrRuO₃ and CaRuO₃ have high RRRs of 15 and 31, respectively, the higher disorder in the $x = 0.4$ and $x = 0.8$ samples enhances the scattering and reduces the RRR to 4 and 5.

The transmittivity and phase response of all samples was investigated in Stuttgart in a THz frequency domain spectrometer with a Mach-Zehnder interferometer^{29,30}. Fig. 2 shows raw data of CaRuO₃ at 300 K and 5 K; for comparison, the transmittivity raw data of an empty NdGaO₃ substrate are also plotted. A frequency range from around 3 cm⁻¹ to 40 cm⁻¹ was covered by measurements with five different backward wave oscillator sources. The prominent Fabry-Pérot type oscillations in the transmitted signal are typical to the raw data of metallic thin films on dielectric substrates and caused by the substrate, as indicated schematically in the inset of Fig. 2. The contribution of the film is a modulation of these substrate resonances: the difference between the data of bare NdGaO₃ and CaRuO₃ on NdGaO₃ in Fig. 2(a) is caused by the film. While the pure NdGaO₃ spectra are almost temperature independent, there is a strong temperature dependence in the thin-film samples. Already in the raw data we see a considerably lower transmittivity at 5 K than at 300 K due to an increased conductivity in the metallic film. The optical conductivity is evaluated directly from the raw data: since both transmittivity and phase are measured, no Kramers-Kronig analysis is required. Each Fabry-Pérot maximum is analyzed to obtain the complex conductivity σ_1 and σ_2 at its peak frequency.^{16,30} From these values, a frequency-dependent scattering rate $\Gamma(\omega)$ can be calculated using the extended Drude formalism:

$$(3) \quad \frac{\Gamma(\omega)}{\omega_P^2} = \frac{\rho_1(\omega)}{4\pi} = \frac{1}{4\pi} \frac{\sigma_1(\omega)}{\sigma_1(\omega)^2 + \sigma_2(\omega)^2}$$

with $\omega_P^2 = 4\pi ne^2/m$ being the plasma frequency, e and m the (free-)electron charge and mass and n the charge carrier density.^{16,31}

III. RESULTS

Fig. 3 shows the frequency-dependent real and imaginary parts of the conductivity of all samples. The absolute values of σ_1 are characteristic of metals and of the order of $10^4 \Omega^{-1} \text{ cm}^{-1}$. At temperatures above 100 K, all samples show nearly frequency-independent real and low imaginary parts: the scattering rate exceeds our measured frequency range. A maximum in $\sigma_1(\omega)$ has been observed in the mid-infrared at these temperatures.^{1,7} In our data there is no visible onset of this maximum, $\sigma_1(\omega)$ drops monotonically.³² In Fig. 1 we compare the THz response at our low-frequency limit (in particular the real part ρ_1 of the frequency-dependent resistivity $\hat{\rho}(\omega) = \rho_1(\omega) + i\rho_2(\omega) = 1/\hat{\sigma}(\omega)$) with results from dc

measurements. There is very good agreement between these two data sets. This suggests that at least in this temperature range there are no additional features in the optical conductivity at lower frequencies. Considering that dc resistivity current paths and THz beam spots probe do not necessarily probe the same sample areas, Fig. 1 also documents the homogeneity of the films.

A. SrRuO₃

The σ_1 and σ_2 spectra of SrRuO₃ for exemplary temperatures are shown in Fig. 3 (a) and (e), respectively. The σ_1 spectrum, rather flat at high temperatures, changes upon cooling; below 40 K, $\sigma_1(\omega)$ develops a drop towards higher frequencies that moves to lower frequencies, down to around 12 cm⁻¹ with decreasing temperature. In terms of the Drude model the drop indicates the scattering rate $\Gamma/2\pi$. To be consistent with a Drude interpretation, $\sigma_2(\omega)$ should show a maximum at the corresponding frequency, passing through our spectral range as a function of temperature³³ and leaving monotonous frequency-dependent behavior in the limiting cases, namely increasing for high temperatures and decreasing for low temperatures, as found in our data. To address the low-temperature properties of SrRuO₃ in more detail, Fig. 4 shows $\sigma_1(\omega)$ for all measured temperatures below 40 K. In addition, we show Drude fits following eq. 1 for a few temperatures. Within the measurement accuracy, the Drude fits describe the conductivity data well above 20 K. However, at lower temperatures, the conductivity of SrRuO₃ deviates from the Drude fit because at high frequencies $\sigma_1(\omega)$ is not reduced further but remains constant.

This plateau for frequencies above 20 cm⁻¹ is present in all spectra of Fig. 4 and becomes more evident with decreasing temperature. Since the plateau cannot be described as part of a single Drude term, the fit at 5 K only includes the points below 30 cm⁻¹. For further analysis we use the extended Drude formalism, eq. 3. The obtained scattering rate is shown in Fig. 5(a) for the same temperatures as in Fig. 3. Above 40 K the scattering rate is basically constant as a function of frequency, corresponding to a simple Drude behavior. Below 20 K, Fig. 5(a) indicates a pronounced frequency dependence of the scattering rate, an increase towards higher frequencies.

Deviations from Drude behavior were noticed earlier by Dodge *et al.*⁶. Our $\sigma_1(\omega)$ of SrRuO₃ qualitatively follows this: flat for high temperatures with a broad low-frequency peak emerging at lowest temperatures. The high quality of our samples, achieved with MAD²², leads to 2-3 times higher absolute values of σ_1 at low temperatures compared to earlier experiments⁶, which enables us to characterize those deviations in better detail.

For this purpose we turn to Fig. 6, where the scattering rate at 5 K is plotted. It is mostly frequency independent below 20 cm⁻¹, in the range below the plateau in $\sigma_1(\omega)$. Above 20 cm⁻¹ it increases strongly with

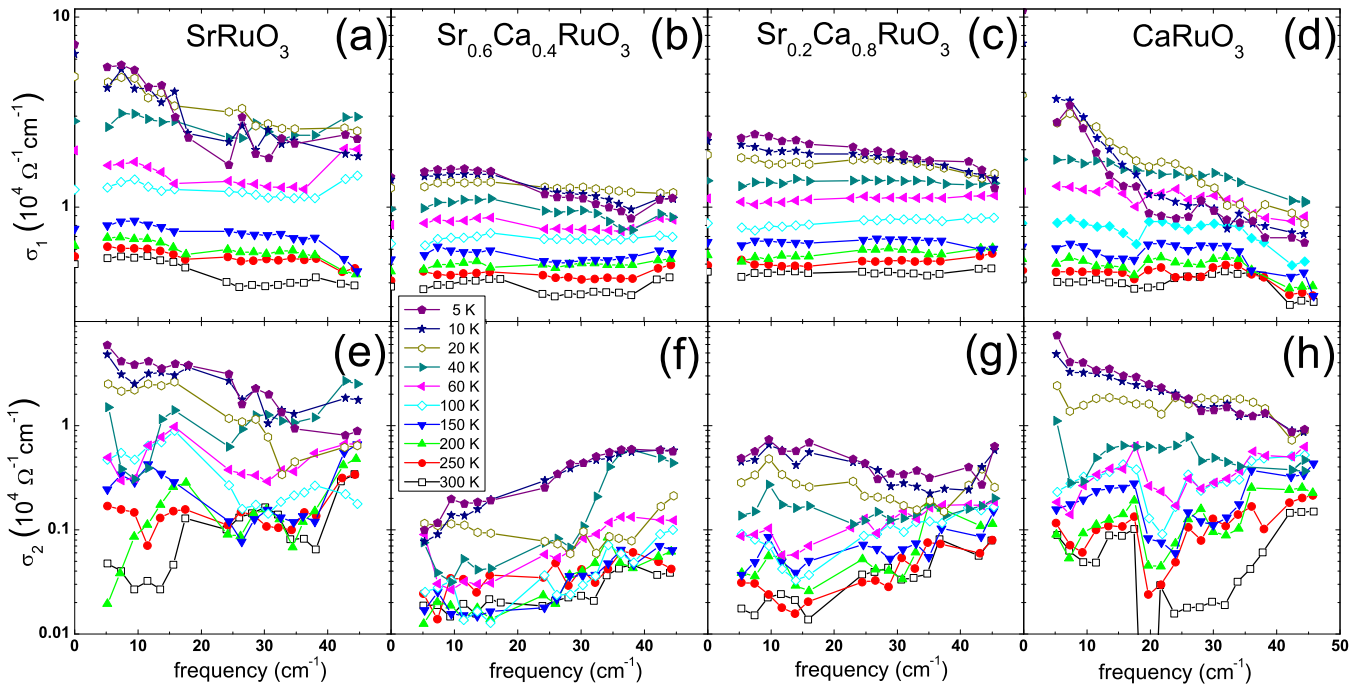


FIG. 3. (Color online) Real and imaginary parts of the optical conductivity of the four studied $\text{Sr}_{1-x}\text{Ca}_x\text{RuO}_3$ compositions at various temperatures between 300 K and 5 K.³²

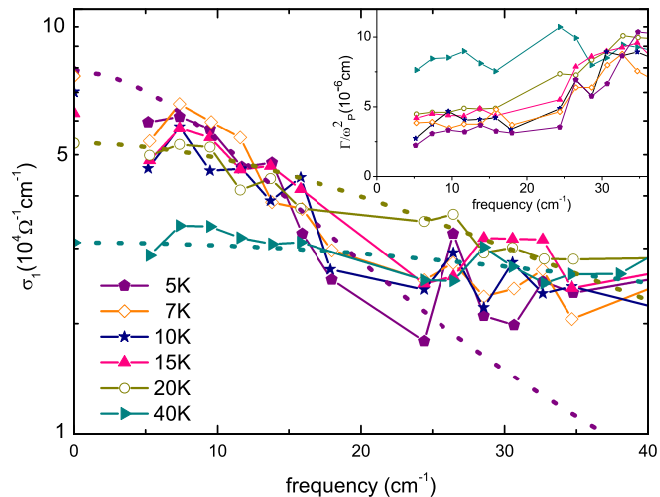


FIG. 4. (Color online) $\sigma_1(\omega)$ of SrRuO_3 for low temperatures. The dotted lines at 5 K, 20 K, and 40 K are Drude fits following eq. 1 with σ_{dc} values fixed from dc measurements. All points were taken into account for the 20 K and 40 K fits, the 5 K fit includes only frequencies below 30 cm^{-1} due to the non-Drude-like plateau at higher frequencies. Inset: Scattering rates for corresponding temperatures.

frequency, approximately by a factor of three between 20 cm^{-1} and 35 cm^{-1} . This increase roughly corresponds to a quadratic FL-like frequency dependence, as indicated by the straight line in Fig. 6. However, the transition from a flat to a steep slope in this double-

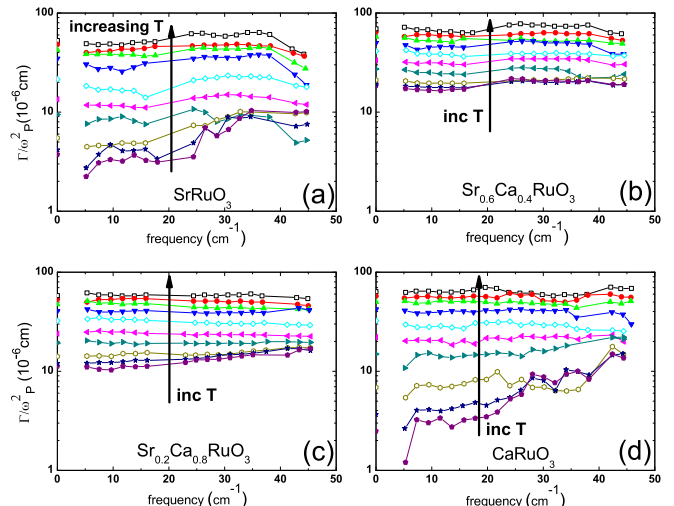


FIG. 5. (Color online) Frequency-dependent scattering rates at 300 K, 250 K, 200 K, 150 K, 100 K, 60 K, 40 K, 20 K, 10 K, and 5 K. Colors and symbols identical to Fig. 3.³⁴

logarithmic plot is much too abrupt to fit the FL prediction $\Gamma(\omega) = \Gamma(\omega = 0) + b(\hbar\omega)^2$ in the entire frequency range. Clearly, simple Fermi-liquid considerations are not sufficient to explain the observed low-temperature frequency dependence of the scattering rate. The low-lying interband transitions¹⁸ that can reproduce such a steep onset of optical scattering rate are discussed in Sec. IV.

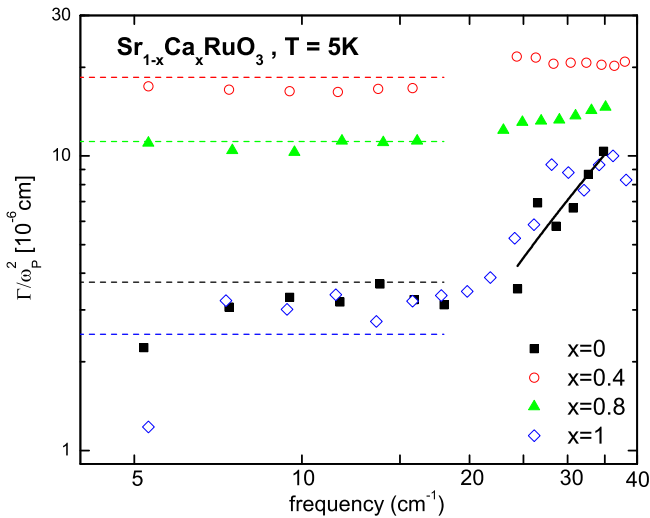


FIG. 6. (Color online) Scattering rates of $\text{Sr}_{1-x}\text{Ca}_x\text{RuO}_3$ at temperature 5 K. The dashed guides indicate the value of the dc scattering rate, which is proportional to $1/\sigma_{\text{dc}}$. The black straight line is the best FL fit, $\Gamma = \Gamma_0 + a\omega^2$ to the high-frequency range of the SrRuO_3 above 20 cm^{-1} .

B. $\text{Sr}_{0.6}\text{Ca}_{0.4}\text{RuO}_3$ and $\text{Sr}_{0.2}\text{Ca}_{0.8}\text{RuO}_3$

The conductivity spectra of the doped samples are shown in Fig. 3 (b), (c), (f), and (g). For both compositions, $\sigma_1(\omega)$ is almost constant, and σ_2 is much smaller than σ_1 ; this suggests a conventional metallic conductivity where the scattering rate is much higher than the studied spectral range. A weak frequency dependence only emerges at the lowest temperatures. Upon cooling, both $\sigma_1(\omega)$ and $\sigma_2(\omega)$ increase, which is consistent with a decrease in scattering rate. From the comparison of all samples in Fig. 3 we find that the conductivity of the doped samples is substantially lower than of the undoped ones. This we attribute to compositional disorder, which significantly increases the residual scattering. As expected, this effect is more pronounced for $\text{Sr}_{0.6}\text{Ca}_{0.4}\text{RuO}_3$, where the disorder due to the composition will be particularly strong. This scenario is consistent with the comparatively small increase of the conductivity upon cooling, and correspondingly with the small residual resistivity ratio. Unlike in the undoped samples there is no strong roll-off in $\sigma_1(\omega)$ at low frequencies. The extended Drude analysis yields a mostly frequency-independent scattering rate (Fig. 5), substantially higher at low temperatures than in the pure compounds (Fig. 6). Therefore the strong disorder scattering in the doped samples dominates their transport properties at low temperatures, which makes it impossible to deduce signatures of electronic correlations from the THz data at this stage. This is unfortunate, as $\text{Sr}_{0.2}\text{Ca}_{0.8}\text{RuO}_3$ is located close to the QPT from ferromagnetism to paramagnetism, and here the influence of quantum-critical fluctuations to the electronic scattering would be of par-

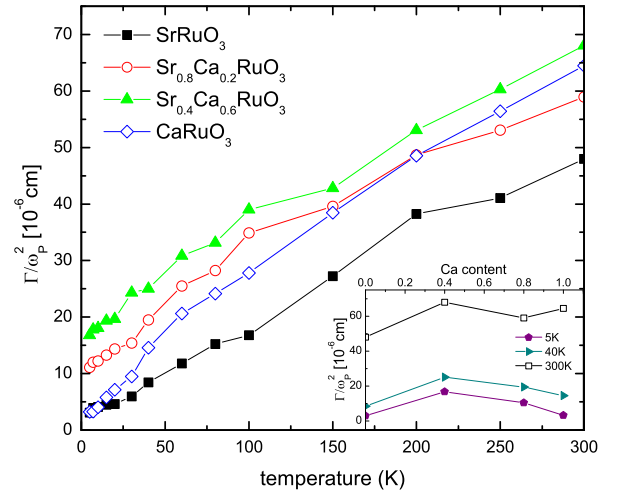


FIG. 7. (Color online) Scattering rate Γ from extended Drude analysis at frequency 7 cm^{-1} for the four different compositions $\text{Sr}_{1-x}\text{Ca}_x\text{RuO}_3$ as a function of temperature (main plot) and as a function of Ca content x (inset).

ticular interest.

That the high scattering rate at low temperatures in these two samples indeed stems from the disorder is illustrated by a comparison with the pure compounds in Fig. 7. The main plot shows the scattering rate as a function of temperature, determined from the extended Drude analysis at 7 cm^{-1} , for all samples of this study. The scattering rates of $\text{Sr}_{0.6}\text{Ca}_{0.4}\text{RuO}_3$ and $\text{Sr}_{0.2}\text{Ca}_{0.8}\text{RuO}_3$ basically are shifted to higher values when compared to SrRuO_3 , and this temperature-independent offset is stronger for $\text{Sr}_{0.6}\text{Ca}_{0.4}\text{RuO}_3$. The inset of Fig. 7 shows the scattering rate as a function of Ca content x for three exemplary temperatures. At the lower temperatures, the dome-shape dependence with minimal scattering for the pure compounds at the two outer ends and a maximum around the center is evident.

C. CaRuO_3

CaRuO_3 exhibits a similar behavior as SrRuO_3 : at high temperatures, $\sigma_1(\omega)$ is almost constant throughout our spectral range and $\sigma_2(\omega)$ is very small (see Fig. 3(d) and (h)). This is consistent with a frequency-independent scattering rate as shown in Fig. 5(d). Upon cooling, σ_1 and σ_2 continuously increase; down to approximately 40 K the frequency dependence of $\sigma_1(\omega)$ as well as $\Gamma(\omega)$ is weak. This changes at lower temperatures (see Fig. 8): at frequencies below 10 cm^{-1} , σ_1 strongly increases while at higher frequencies it is rather constant or even slightly decreasing. At the lowest temperatures, e.g. 5 K, this leads to a pronounced roll-off in $\sigma_1(\omega)$ between 5 cm^{-1} and 10 cm^{-1} , followed by a non-Drude-like plateau. The

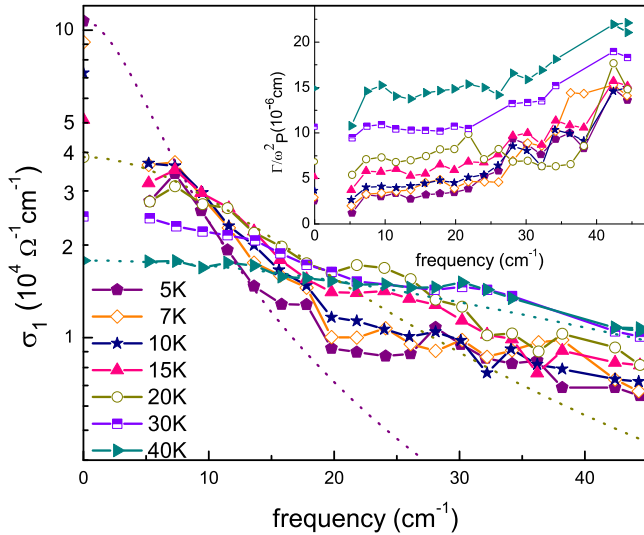


FIG. 8. (Color online) σ_1 spectra of CaRuO₃ for low temperatures with tentative Drude fits. Due to the high-frequency plateau, the fits do not work at lowest temperatures. Inset: Scattering rates for corresponding temperatures.

frequency-dependent scattering rate, extracted from the extended Drude analysis, is shown in in Fig. 5(d), and the 5 K one is compared to the other compositions in Fig. 6.

The optical data on CaRuO₃ was discussed earlier by Schneider *et al.*,¹⁷ and it was found to be inconsistent with Drude or FL behavior³⁵ above 15 cm⁻¹ or so. The deviations from Drude behavior are displayed also on Fig. 8. The high quality of the CaRuO₃ sample is evident from the low scattering rate at lowest temperatures, as clearly discernible from the comparison with the other samples in Fig. 7. With increasing temperature, this low-frequency scattering rate increases more strongly than for SrRuO₃ (and the intermediate samples) due to stronger electronic correlations in the absence of ferromagnetism³⁷.

In previous optical studies on CaRuO₃, Lee *et al.* mainly focused on data above 40 cm⁻¹ in a large temperature range without measuring many low temperatures⁷. This study has substantial overlap in temperature and frequency range with Kamal *et al.*⁸. Our conductivity spectra match these two previous works well and are consistent if quantitative shifts due to our enhanced film quality are taken into account. In our study, the most pronounced frequency and temperature dependence of the conductivity is located at the lowest energies: temperatures below 20 K and frequencies below 10 cm⁻¹, beyond the limits of the previous works. Scaling plots were proposed and were controversially discussed in Lee *et al.*⁷ and Kamal *et al.*⁸. To compare with these earlier works, we replotted our data in the suggested form, see Appendix. Our data on SrRuO₃ does not scale well. For CaRuO₃, the scaling seems to be obeyed, but as was discussed in Ref. 8, the accessible frequency and temper-

ature ranges are too narrow and the noise level too high to draw any firm conclusions.

IV. LOW FREQUENCY OPTICAL CONDUCTIVITY WITHIN LDA

Very recently it was argued that low-lying optical interband transitions, which are activated by orthorhombic distortions, might affect the optical response at unexpectedly low frequencies. In particular, a dynamical mean-field theory (DMFT) study¹⁸ argued that the low frequency deviation from Drude optics in CaRuO₃ occurs already at the level of band theory. As a test for the effects of the band structure in the simplest possible setting, we calculated the optical conductivity of SrRuO₃ and CaRuO₃ (in their bulk structure) using LDA as implemented in the Wien2k package.^{38,39} In this approach, the current matrix elements are evaluated from the band structure and the optical conductivity is evaluated for a frequency-independent scattering rate as described by a self energy $\Sigma = -i(1/\tau_D)/2$. Similar approach was used in iron-based superconductors^{40,41} where also interband contributions were found to be important.

The frequency-dependent real part of the optical conductivity, normalized to the zero-frequency value, is displayed in Fig.9. One sees that the calculated optical conductivities for orthorhombic structures deviate from the Drude behavior $\sigma_1(\omega)/\sigma_{dc} = 1/(1 + \omega^2\tau_D^2)$ at very low frequencies of the order of 20 meV. These deviations originate in low-lying interband transitions across mini-gaps that are opened up by orthorhombic distortions. Nonmagnetic SrRuO₃ shows very similar behavior to CaRuO₃ but with obvious deviations from Drude behavior at even lower frequencies, which is due to the fact that the orthorhombic distortion is smaller there. The shift of the bands due to the exchange splitting in ferromagnetic SrRuO₃ (with moment 1.6 μ_B) diminishes these deviations. The calculated optical conductivity in the cubic structure deviates from the Drude behavior starting at a higher frequency and in a much less pronounced way.

For easier comparison with the experimental data, we extracted also $\rho_1(\omega) = \text{Re}(1/\hat{\sigma}(\omega))$, which is proportional to the optical scattering rate as defined by the extended Drude formalism. This presents a very clear influence of the band-structure effect. Although the actual scattering rate put into the calculation is frequency independent, the inferred optical scattering rate (that attempts to describe the response of a multi-band system in terms of the response of a single-band one) exhibits a strong frequency dependence.

In these calculations, SrRuO₃ and CaRuO₃ show a deviation from the Drude dynamics at a similar frequency of about 20 meV. To compare this value to the frequency in the experiment, one needs to additionally divide the value by the corresponding renormalizations. In CaRuO₃, the measured specific heat is about 7 times above the value found in the band theory.⁴² Therefore

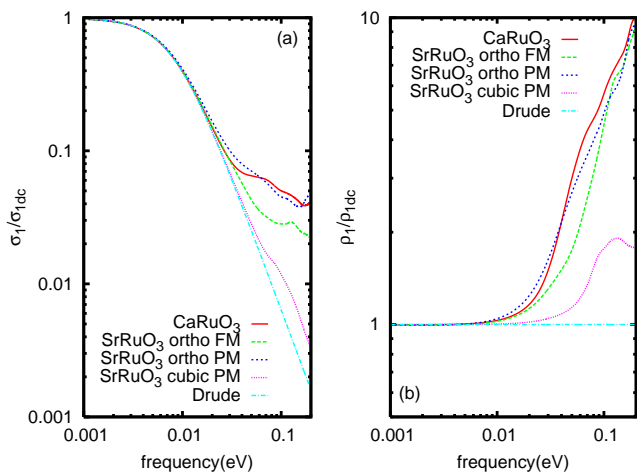


FIG. 9. (Color online)(left) Optical conductivity in the LDA approximation with static impurity scattering $1/\tau_D = 0.008$ eV for CaRuO₃ and for SrRuO₃ compared to the Drude optical conductivity. For SrRuO₃ besides ferromagnetic calculation in an orthorhombic structure also the paramagnetic result in the orthorhombic and cubic structure are shown. (right) The corresponding optical scattering rates, normalized to the dc value.

the expected frequency for the deviation from Drude dynamics is $20 \text{ meV}/7 \approx 3 \text{ meV}$ ($\approx 0.7 \text{ THz} \approx 24 \text{ cm}^{-1}$) and consistent with the experiment.

In SrRuO₃ the renormalization is smaller, about 4 judging from the specific heat.⁴³ Furthermore, mostly the minority carriers (with the plasma frequency $\omega_{p\downarrow} \sim 2.6$ eV) and not the majority carriers (that correspond to small Fermi surfaces of the almost completely filled bands and the plasma frequency $\omega_{p\uparrow} \sim 1.3$ eV) contribute to the conductivity and within LDA+DMFT it was found¹⁸ that the renormalization for these minority carriers is smaller, only about 2.

From these considerations, the deviation from Drude behavior through band structure effects would only be expected at a frequency scale above our experimental range. However, one needs to keep in mind that the growth of SrRuO₃ on NdGaO₃ substrate modifies the structure substantially^{23,24}, which may decrease the corresponding scale. This should be tested in future theoretical calculations or experimentally by growth on different substrates.

V. CONCLUSIONS AND OUTLOOK

The optical conductivity of the four samples SrRuO₃, Sr_{0.6}Ca_{0.4}RuO₃, Sr_{0.2}Ca_{0.8}RuO₃, and CaRuO₃ of the material system Sr_{1-x}Ca_xRuO₃ with a QPT at $x \approx 0.8$ were investigated with THz spectroscopy. The transmittivity and phase data revealed metallic behavior for all samples. The doped samples have a comparably high

scattering rate due to compositional disorder, and their THz properties can be described within a simple Drude picture. The SrRuO₃ and CaRuO₃ samples, in contrast, at low temperatures have low scattering rates consistent with the high RRRs that could be achieved by MAD growth. At low temperatures, SrRuO₃ and CaRuO₃ can be described by a Drude response with constant scattering rate only up to approximately 20 cm^{-1} . By calculating the optical response within the band theory we have shown that the deviations from Drude behavior may be caused by low-lying interband transitions. Especially for CaRuO₃ the calculated response is very similar to the measured one, whereas for SrRuO₃ the calculated scattering rate deviates at a frequency that is too high to account for our measurements. A possible origin of this discrepancy is a deviation of the thin-film structure from the bulk-one for which the calculations were made, an issue that needs to be explored in future work.

On the experimental side, future studies should on the one hand attempt to reach lower temperatures^{30,44,45} and frequencies^{46,47} in particular to check if the crossover to a scattering rate quadratic in frequency that would indicate the elusive FL optical response^{31,48-51} can be found. Furthermore, optical measurements on our MAD-grown samples at higher frequencies, in the infrared range, should be performed to allow direct comparison with previous studies of samples with somewhat lower RRR at infrared frequencies and to further investigate the nature of the non-Drude plateau. At these larger frequencies not only the band-effects but also the genuine contribution from correlations¹⁸ will contribute.

Further improvement in sample growth can be envisaged, too. While the scattering rate for doped samples with random arrangement of Sr and Ca atoms will remain too high to reveal interesting behavior in our frequency range, further improvements of the residual scattering of CaRuO₃ thin films have recently been achieved by growth on NdGaO₃ substrates with vicinal cut¹⁷. THz studies on such samples might be more difficult due to birefringence in the substrate,^{52,53} but finally such studies might reveal even more clearly the unconventional scattering rate of CaRuO₃ at THz frequencies.

VI. APPENDIX - SCALING ANALYSIS

Previous optical studies found that $\sigma_1(\omega, T)$ data for SrRuO₃ and CaRuO₃ can be combined into a scaling plot following eq.

$$(4) \quad \sigma_1(\omega, T) = \omega^{-1/2} Z(\omega/T)$$

with scaling function $Z(\omega/T)$.^{7,8} Such scaling of an experimentally accessible response can be a strong indication for quantum-critical behavior,^{54,55} but the initial suggestion⁷ that the apparent scaling of $\sigma_1(\omega, T)$ in SrRuO₃ and CaRuO₃ should be interpreted as quantum critical was later rebutted.⁸ To present our data in the context of the scaling analysis of those previous works,

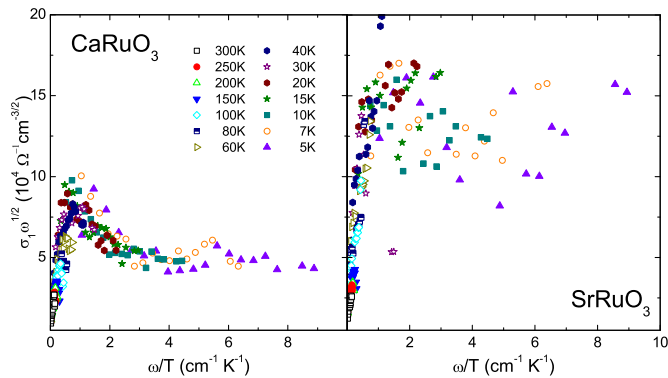


FIG. 10. ω/T scaling plots for SrRuO₃ and CaRuO₃ following Refs. 8 and 7

we plot $\sigma_1(\omega, T)\omega^{1/2}$ vs. ω/T in Fig. 10, which should lead to data collapse if eq. 4 were appropriate to describe the data. While our high-temperature spectra collapse into a small region of the scaling plot for both samples, below 40 K the samples differ strongly: in the case of CaRuO₃, within the experimental error, all temperatures collapse to one scaling curve, which slightly broadens for lower temperatures. For SrRuO₃ the spectra fail to collapse below 40 K. Although CaRuO₃ and SrRuO₃ show similar features in their optical conductivities and scattering rates, they are different with respect to the low-energy scaling behavior. Our low-frequency and low-temperature spectra of SrRuO₃ cannot be scaled by expression 4, while it works well for CaRuO₃.

- * present address: Experimentalphysik VI, Center for Electronic Correlations and Magnetism, Institute for Physics, Augsburg University, D-86135 Augsburg, Germany
- † marc.scheffler@pi1.physik.uni-stuttgart.de
- ¹ D. N. Basov, R. D. Averitt, D. van der Marel, M. Dressel, and K. Haule, *Rev. Mod. Phys.* **83**, 471 (2011).
 - ² T. Vojta, *Ann. Phys.* **9**, 403 (2000).
 - ³ H. v. Löhneysen, A. Rosch, M. Vojta, P. Wölfle, *Rev. Mod. Phys.* **79**, 1015 (2007).
 - ⁴ F. P. Mena, D. van der Marel, A. Damascelli, M. Fth, A. A. Menovsky, J. A. Mydosh *Phys. Rev. B* **67**, 241101 (2003).
 - ⁵ P. Kostic, Y. Okada, N. C. Collins, Z. Schlesinger, J. W. Reiner, L. Klein, A. Kapitulnik, T. H. Geballe, M. R. Beasley, *Phys. Rev. Lett.* **81**, 2498 (1998).
 - ⁶ J. S. Dodge, C. P. Weber, J. Corson, J. Orenstein, Z. Schlesinger, J. W. Reiner, M. R. Beasley, *Phys. Rev. Lett.* **85**, 4932 (2000).
 - ⁷ Y. S. Lee, J. Yu, J. S. Lee, T. W. Noh, T. H. Gimm, H. Y. Choi, C. B. Eom, *Phys. Rev. B* **66**, 041104 (2002).
 - ⁸ S. Kamal, D. M. Kim, C. B. Eom, J. S. Dodge, *Phys. Rev. B* **74**, 165115 (2006).
 - ⁹ G. Cao, S. McCall, M. Shepard, J. E. Crow, *Phys. Rev. B* **56**, 321 (1997).
 - ¹⁰ P. Khalifah, I. Ohkubo, H. M. Christen, D. G. Mandrus, *Phys. Rev. B* **70**, 134426 (2004).
 - ¹¹ D. Fuchs, C.L. Huang, J. Schmalian, M. Wissinger, S. Schuppler, K. Grube, and H. v. Löhneysen, *Eur. Phys. J. Special Topics* **224**, 1105 (2015).
 - ¹² G. Koster, L. Klein, W. Siemons, G. Rijnders, J. S. Dodge, C. B. Eom, D. H. A. Blank, and M. R. Beasley, *Rev. Mod. Phys.* **84**, 253 (2012).
 - ¹³ L. Capogna, A. P. Mackenzie, R. S. Perry, S. A. Grigera, L. M. Galvin, P. Raychaudhuri, A. J. Schofield, C. S. Alexander, G. Cao, S. R. Julian, Y. Maeno, *Phys. Rev. Lett.* **88** (2002) 076602.
 - ¹⁴ G. Cao, O. Korneta, S. Chikara, L. E. DeLong, P. Schlottmann, *Sol. State. Comm.* **148** (2008) 305.
 - ¹⁵ A. P. Mackenzie, J. W. Reiner, A. W. Tyler, L. M. Galvin, S. R. Julian, M. R. Beasley, T. H. Geballe, A. Kapitulnik, *Phys. Rev. B* **58** (1998) 13318(R).

- ¹⁶ M. Dressel and G. Grüner *Electrodynamics of Solids*, Cambridge University Press (2002).
- ¹⁷ M. Schneider, D. Geiger, S. Esser, U. S. Pracht, C. Stingl, Y. Tokiwa, V. Moshnyaga, I. Sheikin, J. Mravlje, M. Scheffler, and P. Gegenwart, *Phys. Rev. Lett.* **112**, 206403 (2014).
- ¹⁸ H. T. Dang, J. Mravlje, A. Georges, and A. J. Millis, *Phys. Rev. Lett.* **115**, 107003 (2015).
- ¹⁹ D. Stricker, J. Mravlje, C. Berthod, R. Fittipaldi, A. Vecchione, A Georges, and D. van der Marel, *Phys. Rev. Lett.* **113**, 087404 (2014).
- ²⁰ M. Schneider, V. Moshnyaga, and P. Gegenwart, *Phys. Status Solidi B* **247**, 577 (2010).
- ²¹ A. Sidorenko, P. Petrenko, A. Weidinger, M. Zeitler, B. Rauschenbach, R. Tidecks, K. Samwer, V. Moshnyaga, and I. Khoroshun, *Appl. Phys. Lett.* **74**, (1999).
- ²² M. Schneider, V. Moshnyaga, P. Gegenwart, *J. Phys.: Conf. Ser.* **200**, (2010).
- ²³ R. Aso, D. Kan, Y. Shimakawa, H. Kurata, *Cryst. Growth Des.* **14**, 2128, (2014).
- ²⁴ A. T. Zayak, X. Huang, J. B. Neaton, K. M. Rabe *Phys. Rev. B* **77** 214410, (2008).
- ²⁵ W. Lu, W. Song, P. Yang, J. Ding, G. Moog Chow, and J. Chen, *Scientific Reports* **5**, 10245 (2015).
- ²⁶ A. Vailionis, W. Siemons, G. Koster, *Appl. Phys. Lett.* **93**, 051909 (2008).
- ²⁷ D. Geiger, M. Scheffler, M. Dressel, M. Schneider, P. Gegenwart, *J. Phys.: Conf. Ser.* **391**, 012091 (2012).
- ²⁸ M. M. Felger, M. Dressel, M. Scheffler *Rev. Sci. Instrum.* **84**, 114703 (2013).
- ²⁹ B. P. Gorshunov, A. A. Volkov, A. S. Prokhorov, I. E. Spektor, *Phys. Solid State* **50**, 2001 (2008).
- ³⁰ U. S. Pracht, E. Heintze, C. Clauss, D. Hafner, R. Bek, S. Gelhorn, D. Werner, M. Scheffler, M. Dressel, D. Sherman, B. Gorshunov, K. S. Il'in, D. Henrich, M. Siegel, *IEEE Trans. THz Sci. Technol.* **3**, 269 (2013).
- ³¹ M. Scheffler, K. Schlegel, C. Clauss, D. Hafner, C. Fella, M. Dressel, M. Jourdan, J. Sichelschmidt, C. Krellner, C. Geibel, F. Steglich, *Phys. Status Solidi B* **250**, 439 (2013).
- ³² Our measured data start with dc measurements ($f = \omega/2\pi = 0$), followed by frequencies from around 5 cm^{-1}

- to 40 cm^{-1} . We find that at the lowest frequencies it becomes increasingly difficult to obtain precise values for the conductivity because of stray radiation: a fraction of the comparatively broad THz beam can reach the detector without interfering with the sample and therefore cause a higher experimentally determined transmittivity. This becomes most evident at high conductivity values because the absolute signal strength is already very low. In our measurements with highest σ_1 (found in the undoped samples at low temperatures) the lowest frequency point is lower than expected. We attribute this feature to stray radiation and do not interpret it in terms of a physical property of the sample.
- ³³ M. Dressel and M. Scheffler, *Ann. Phys. (Leipzig)* **15**, 535 (2006).
- ³⁴ At the highest frequencies, correspondingly at the shortest wavelength, the THz phase measurement is more difficult, thus leading to less reliable data in σ_2 and Γ , which in our case might be particularly the case for the measurements on the rather thick SrRuO₃ sample, with its low overall THz transmitted signal, above 40 cm^{-1}
- ³⁵ C. Berthod, J. Mravlje, X. Deng, R. Žitko, D. v. d. Marel, and A. Georges *Phys. Rev. B* **87**, 115109 (2013)
- ³⁶ K. Yoshimura, T. Imai, T. Kiyama, K. R. Thurber, A. W. Hunt, K. Kosuge, *Phys. Rev. Lett.* **83**, 4397 (1999).
- ³⁷ H. T. Dang, J. Mravlje, A. Georges, A. J. Millis, *Phys. Rev. B* **91**, 195149 (2015).
- ³⁸ P. Blaha, K. Schwarz, G. Madsen, D. Kvasnicka, and J. Luitz, WIEN2k, An Augmented Plane Wave + Local Orbitals Program for Calculating Crystal Properties (Technische Universität Wien, Vienna, 2001).
- ³⁹ C. Ambrosch-Draxl and J. Sofo, *Comp. Phys. Comm.* **175**, 1 (2006).
- ⁴⁰ L. Benfatto, E. Cappelluti, L. Ortenzi, L. Boeri, *Phys. Rev. B* **83**, 224514 (2011).
- ⁴¹ M. J. Calderon, L. de Medici, B. Valenzuela, E. Bascone, *Phys. Rev. B* **90**, 115128 (2014).
- ⁴² M. Shepard, S. McCall, G. Cao, J. E. Crow, *J. Appl. Phys.* **81**, 4978 (1997).
- ⁴³ P. B. Allen, H. Berger, O. Chauvet, L. Forro, T. Jarlborg, A. Junod, B. Revaz, G. Santi, *Phys. Rev. B* **53**, 4393 (1996).
- ⁴⁴ N. Bachar, U. S. Pracht, E. Farber, M. Dressel, G. Deutscher, and M. Scheffler, *J. Low. Temp. Phys.* **179**, 83 (2015).
- ⁴⁵ D.N. Basov, S.V. Dordevic, E.J. Singley, W.J. Padilla, K.S. Burch, J.E. Elenewski, L.H. Greene, J. Morris, and R. Schickling, *Rev. Sci. Instrum.* **74**, 4703 (2003).
- ⁴⁶ M. Scheffler and M. Dressel, *Rev. Sci. Instrum.* **76**, 074702 (2005).
- ⁴⁷ K. Steinberg, M. Scheffler, and M. Dressel, *Rev. Sci. Instrum.* **83**, 024704 (2012).
- ⁴⁸ M. Dressel, *J. Phys.: Condens. Matter* **23**, 293201 (2011).
- ⁴⁹ U. Nagel, T. Uleksin, T. Rõõm, R. P. S. M. Lobo, P. Lejay, C. C. Homes, J. Hall, A. W. Kinross, S. Purdy, T. J. Williams, G. M. Luke, T. Timusk, *PNAS* **109** (2012).
- ⁵⁰ A. V. Chubukov, D. L. Maslov, *Phys. Rev. B* **86**, 155136 (2012).
- ⁵¹ D. L. Maslov, A. V. Chubukov, *Phys. Rev. B* **86**, 155137 (2012).
- ⁵² M. Scheffler, J. P. Ostertag, and M. Dressel, *Opt. Lett.* **34**, 3520 (2009).
- ⁵³ J. P. Ostertag, M. Scheffler, M. Dressel, and M. Jourdan, *Phys. Rev. B* **84**, 035132 (2011).
- ⁵⁴ A. Schröder, G. Aeppli, R. Coldea, M. Adams, O. Stockert, H. v. Löhneysen, E. Bucher, R. Ramazashvili, P. Coleman, *Nature* **407**, 351 (2000).
- ⁵⁵ O. Stockert, H. v. Löhneysen, W. Schmidt, M. Enderle, M. Loewenhaupt, *J. Low Temp. Phys.* **161**, 55 (2010).